ChemComm

COMMUNICATION

View Article Online
View Journal

Cite this: DOI: 10.1039/d6cc02378a

Received 18th April 2026,
Accepted 26th May 2026

DOI: 10.1039/d6cc02378a

rsc.li/chemcomm

Effects of the synthesis route on the structure and electrochemical performance of layered oxide cathodes for Na-ion batteries

Arnob Dey, [a] Sharmin Akter, [a] Arjun Thapa,[b] Jacek B. Jasinski [b] and Hui Wang *[a]

The synthesis route plays a critical role in determining the structural and electrochemical stability of layered oxide cathodes for sodium ion batteries. In this work, using $Na_{0.67}Fe_{0.5}Mn_{0.5}O_2$ as a model layered oxide cathode, we investigate two synthesis methods: co-precipitation and solid-state reaction, to elucidate their influence on the phase, morphology and electrochemical performance. The structural and electrochemical characterization studies reveal that the co-precipitation-derived materials exhibit superior cycling stability and higher reversible capacity compared to their solid-state counterparts. The improved performance is attributed to the formation of a fine, homogeneous morphology and high phase purity. These findings highlight the important role of the synthesis route in controlling particle morphology and phase purity toward high-performance, structurally stable sodium-ion battery cathodes.

Layered transition-metal oxide cathodes, Na_xTMO_2 (TM = Ni, Mn, Co, Fe, *etc*), as counterparts to $LiCoO_2$ used in commercial lithium-ion batteries (LIBs), have emerged as promising cathode materials for cost-effective and large-scale applications of sodium-ion batteries (SIBs).[1,2] Compared with other cathode materials (*e.g.*, phosphates and Prussian blue analogues), Na_xTMO_2 compounds offer several advantages, such as high operating voltage and specific energy density, tuneable structure and composition, *etc.*[3–5] Depending on the stacking sequence of oxygen layers and the coordination environment of Na^+ ions, Na_xTMO_2 cathode materials can adopt various structural types (O3- and P2-types). In O-type structures, Na^+ ions occupy octahedral sites, while they reside in prismatic sites in P-type structures. These structural configurations govern interlayer spacing and Na^+ diffusion pathways, thereby influencing their structural stability, ion diffusion, and electrochemical performance, such as capacity and rate capability.[6]

Due to the use of earth abundant elements, environmental benignity, and high specific capacity, Mn-based layered oxide cathodes (P2- and O3-type) are particularly attractive among various transition metal systems.[4,7,8] However, their cycling stability remains limited due to the complex phase transition during Na^+ extraction,[9] resulting in structural instability, consequent capacity fading and poor rate performance.[10,11] To mitigate these issues, extensive efforts have focused on doping strategies (cation or anion substitution), optimization of Na content and the phase ratio, interface engineering, surface coating, *etc.*[12–15] For instance, Hu *et al.* reported that Mg^{2+} incorporation activates the oxygen redox process in an O3-type $NaFe_{0.5}Mn_{0.5}O_2$ cathode, achieving a high charge capacity of 207 mAh g^{-1}.[16] Qi *et al.* demonstrated that Li/Cu co-doping in a P2-type $Na_{0.65}Li_{0.08}Cu_{0.08}Fe_{0.24}Mn_{0.6}O_2$ cathode enhanced cycling stability (88.2% capacity retention after 500 cycles) and rate performance by reducing volume changes.[17]

In addition to compositional design, the synthesis process also plays a crucial role in influencing the crystallinity, structural integrity and electrochemical performance of Mn/Fe-based layered oxides.[18,19] The popular solid-state synthesis route involves high-temperature calcination (typically 800–1000 °C) of stoichiometric mixtures of sodium and transition-metal precursors in an oxygen-rich atmosphere. Besides, solution-based synthesis approaches (*e.g.*, co-precipitation, sol–gel, spray pyrolysis, *etc.*) are also developed to enable finer control over crystal growth, particle size, and phase purity. The choice of the synthesis method has a significant influence on the crystallographic phase composition (P2-, O3-, or mixed-structure), particle size, and defect concentration of Na-layered oxides, all of which directly affect Na^+ diffusion kinetics and structural reversibility during electrochemical cycling.[20]

Developing effective and scalable synthesis strategies for Mn/Fe-based layered cathodes is crucial to optimizing their electrochemical performance in SIBs. Nevertheless, a systematic comparison between solid-state synthesis and co-precipitation synthesis routes remains rarely reported. Here, $Na_{0.67}Fe_{0.5}Mn_{0.5}O_2$ is employed as a model system due to its earth-abundant composition, balanced

[a] *Mechanical Engineering Department, University of Louisville, Louisville, KY, 40292, USA. E-mail: hui.wang.1@louisville.edu*
[b] *Conn Center for Renewable Energy Research, University of Louisville, Louisville, KY, 40292, USA*

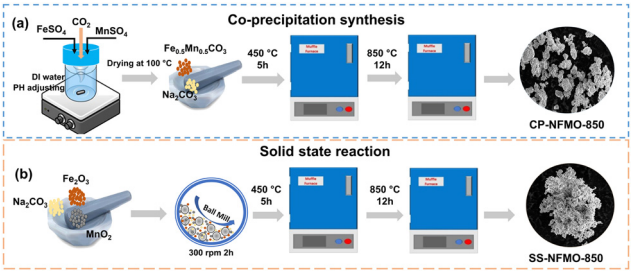

Fig. 1 Schematic of the two synthesis methods: (a) co-precipitation and (b) solid-state synthesis.

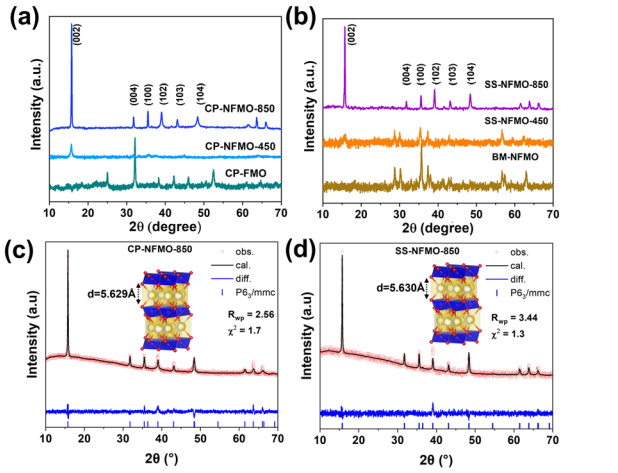

Fig. 2 XRD patterns of intermediate products from (a) the co-precipitation method and (b) the solid-state reaction method; Rietveld refinement results for (c) CP-NFMO-850 and (d) SS-NFMO-850 samples.

Mn/Fe redox activity, and stable P2-type structure. The carbonate co-precipitation and solid-state synthesis routes are comparatively investigated. Detailed structural and morphological characterization studies are performed to elucidate their distinct reaction mechanisms and their impact on phase formation, crystallinity and electrochemical cycling performance.

Fig. 1 illustrates the schemes of co-precipitation and solid-state synthesis routes. In the co-precipitation synthesis (Fig. 1a), two precursor solutions (aqueous 1M $FeSO_4$ and 1M $MnSO_4$) were mixed in a 1 : 1 molar ratio under magnetic stirring and a CO_2 gas flow to facilitate the precipitation of $Fe_{0.5}Mn_{0.5}CO_3$. The resulting precipitate was filtered, washed and dried, followed by a two-step heat treatment (450 °C and 850 °C) with Na_2CO_3 in a stoichiometric ratio of $Na_{0.67}Fe_{0.5}Mn_{0.5}O_2$ (CP-NFMO-850). In the solid-state synthesis (Fig. 1b), stoichiometric amounts of Na_2CO_3, Fe_2O_3, and Mn_2O_3 precursors were thoroughly mixed and ball-milled for 2 hours. The resulting mixture was calcined through a two-step heat treatment (450 °C and 850 °C), then cooled down to room temperature to obtain $Na_{0.67}Fe_{0.5}Mn_{0.5}O_2$ (SS-NFMO-850).

To investigate the synthesis pathways of the two approaches, intermediate products collected at different stages were examined by X-ray diffraction (XRD) and scanning electron microscopy (SEM) to characterize the structural and morphological evolution. Fig. 2a presents the XRD patterns of the co-precipitation derived samples: $Fe_{0.5}Mn_{0.5}CO_3$ (CP-FMO), the product after sodiation at 450 °C (CP-NFMO-450), and that after 850 °C sodiation (CP-NFMO-450), respectively. When synthesized at room temperature and pH < 7, the co-precipitated $Fe_{0.5}Mn_{0.5}CO_3$ (CP-FMO) exhibits characteristic diffraction peaks at 2θ = 32.1°, 42.2°, and 52.5° indexed to a rhombohedral carbonate phase.[21] Upon using Na_2CO_3 as the sodium source and heating at 450 °C, the carbonate peaks disappear, while a new diffraction peak appears at 2θ = 15.7°, indicating the formation of an intermediate layered oxide phase. Notably, this phase has previously been reported to form above 550 °C when NaOH is used as the sodium source,[22] suggesting that the carbonate-assisted reaction pathway facilitates phase formation. After calcination at 850 °C, the CP-NFMO-850 sample exhibits strong diffraction peaks at 2θ = 15.73°, 35.45°, 38.99°, and 48.47°, corresponding to the (002), (100), (102), and (103) planes of the P2-type layered structure (space group: *P*63/*mmc*).

Fig. 2b shows the XRD patterns of the solid-state-derived samples: ball-milled precursors (BM-NFMO), the sample heat-treated at 450 °C (SS-NFMO-450), and the sample calcined at 850 °C (SS-NFMO-850). BM-NFMO displays diffraction peaks corresponding to individual precursors: MnO_2 (2θ = 28.7°, 37.2°), Fe_2O_3 (2θ = 33°, 35°, 37.2°), Na_2CO_3 (2θ = 30°, 35°, 38°), and mixed-phase $FeMn_2O_4$ (2θ = 56.5°, 57.4°, 63°). After heating at 450 °C, the diffraction patterns remain dominated by precursors, except for a minor peak emerging at 2θ = 15.7°, which indicates the initial solid-state sodiation reaction. With increasing heat-treatment temperature to 850 °C, the precursor peaks completely disappear, and new diffraction patterns show similar peaks to those of the CP-NFMO-850 sample. XRD Rietveld refinement results for the synthesized CP-NFMO-850 and SS-NFMO-850 samples are displayed in Fig. 2c and d and Table S1. Both samples predominantly crystallize in a P2-type layered structure, with an interlayer spacing of ~5.630 Å. No O3-type phase is observed for NFMO-850 under either synthesis method, as evidenced by the absence of a diffraction peak at 2θ = 16–17° corresponding to the (003) plane.

The morphological evolution during the co-precipitation process is shown in Fig. 3a–c. The as-prepared CP-FMO precursor exhibits spherical particles. After sodiation at 450 °C and calcination at 850 °C, the dispersed spherical morphology is retained with a uniform particle size. For the solid-state synthesis route (Fig. 3d–f), ball-milled precursors consist of large, irregular aggregates formed by clustering of smaller secondary particles. This morphology remains largely unchanged after heating at 450 °C and calcination at 850 °C, consistent with typical morphologies reported for solid-state synthesized layered oxides.[23] Particle size distribution analysis based on SEM images (Fig. S1) confirms that the CP method produces a narrower size distribution with a particle size of 3–8 μm compared to the broader range of 4–40 μm observed for solid-state synthesis. A finer particle size is considered to be beneficial for electrochemical performance.[24]

High resolution transmission electron microscopy (HRTEM) was further employed to examine the microstructure of the CP-NFMO-850 (Fig. 3g and h) and SS-NFMO-850 samples

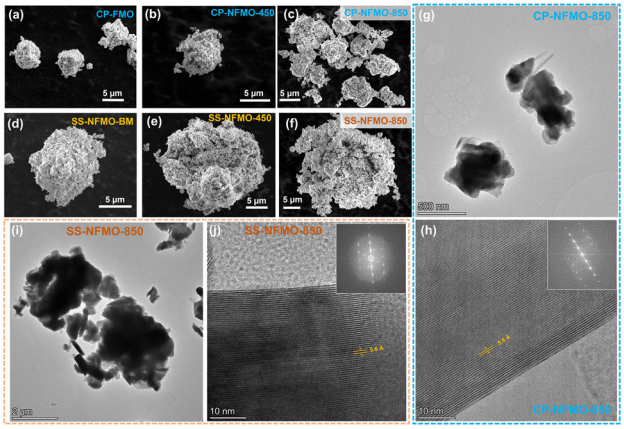

Fig. 3 SEM images of materials synthesized *via* co-precipitation: (a) CP-FMO, (b) CP-NFMO-450 and (c) CP-NFMO-850; SEM images of materials obtained *via* solid-state synthesis: (d) SS-BM, (e) SS-NFMO-450 and (f) SS-NFMO-850; HRTEM and EDX mapping of (g) CP-NFMO-850 and (h) SS-NFMO-850.

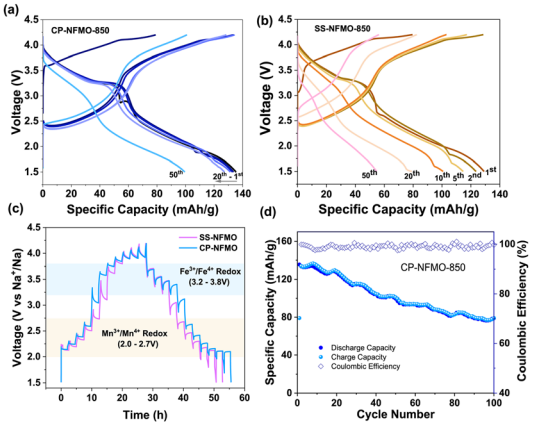

Fig. 4 Charge/discharge profiles of (a) CP-NFMO and (b) SS-NFMO; (c) d*B*/d*V* plots and (d) electrochemical cycling performance of CP-NFMO.

(Fig. 3i and j). The TEM observations are consistent with the SEM analysis, revealing that the CP-derived NFMO sample exhibits smaller and more uniform secondary particles compared to the SS-derived NFMO counterpart. Clear lattice fringes are observed in the high magnification HRTEM images (Fig. 3h and j), with an interlayer spacing of ~5.60 Å, corresponding to the (002) plane of the layered structure. The corresponding FFT patterns (insets), together with the in-plane TEM images and their FFT patterns (Fig. S2), further confirm high crystallinity and a well-ordered P2-type structure. Additional TEM images from different regions, along with EDS-based elemental mapping, are presented in Fig. S3 and S4. The CP-derived NFMO sample shows a uniform elemental distribution of Na, Fe, Mn, and O, consistent with a previous report on an Mn-rich layered oxide cathode synthesized *via* a co-precipitation method.[25] In contrast, the SS-NFMO-850 sample displays a relatively inhomogeneous elemental distribution. Specifically, Na and O are more accumulated at the edge rather than in the centre. This observation is further supported by the EDS spectrum of the SS-NFMO-850 sample (Fig. S5), whereas the atomic fraction of Na (7.07%) is much less than that of Mn (20.91%) and Fe (21.83%). The observed Na deficiency is related to Na loss caused by high temperature calcination in the solid-state synthesis method.[26] In comparison, the CP-derived sample exhibits higher Na content (12–15%, Fig. S6).

Both CP-NFMO-850 and SS-NFMO-850 samples were employed to assemble half-cells with Na metal as the anode using a liquid electrolyte (1 M $NaPF_6$ in EC/DMC at a 1 : 2 volume ratio with 5 vol% FEC). Fig. 4a presents the galvanostatic charge–discharge profile of the CP-NFMO-850 sample cycled in a voltage window of 1.5–4.2 V. The cell delivers an initial specific discharge capacity of 135 mAh g^{-1} at 1C (1C = 140 mAh g^{-1}). Then the specific capacity slightly drops to 128 mAh g^{-1} at the 20th cycle and to 100 mAh g^{-1} at the 50th cycle, indicating relatively stable cycling. In contrast, the cell with the SS-NFMO-850 cathode exhibits not only a lower initial specific capacity (127 mAh g^{-1} at 1C) but also rapid capacity fading (Fig. 4b). Notably, the capacity drops below 80 mAh g^{-1} after 20 cycles. Similar rapid degradation has been reported in solid-state synthesised NFMO at various calcination temperatures (850–1000 °C) at 0.1C.[23] This comparison reveals that the CP-NFMO cathode shows superior structural and electrochemical stability compared to SS-NFMO. Table S2 compares the electrochemical performance between the present CP-NFMO and previously reported NFMO cathodes.

The differential capacity (d*Q*/d*V*) plots further elucidate the capacity-fading mechanism in these two samples (Fig. S7). Three pairs of redox peaks are observed, including the Mn^{3+}/Mn^{4+} redox region at 2.0–2.7 V, the Fe^{3+}/Fe^{4+} redox region at 3.2–3.8 V, and the peaks beyond 4.0 V due to oxygen redox.[15] During cycling, the CP-NFMO-850 cathode exhibits obvious redox peaks (blue curves) and narrower polarization from the 2nd to the 20th cycle compared to the SS-NFMO-850 sample (pink curves). A detailed comparison of the 2nd, 3rd, 5th, 10th, and 20th cycles (Fig. S8) reveals this trend more obviously: minor polarization increases are observed for the CP-NFMO cathode, while a rapidly diminishing peak is observed for the SS-NFMO sample. These results reveal that the co-precipitation method effectively enhances redox reversibility compared to the conventional solid-state synthesis of the NFMO cathode.

To further investigate the Na^+ ion diffusion kinetics, the galvanostatic intermittent titration technique (GITT) was used. As shown in Fig. 4c, higher voltage plateaus are observed for the CP-NFMO electrode in both charge and discharge cycles within the Mn^{3+}/Mn^{4+} and Fe^{3+}/Fe^{4+} redox regions, which is beneficial for achieving higher energy density.[27] Furthermore, the average Na^+ diffusion coefficient of CP-NFMO during the discharge process is 1.84×10^{-9} cm^2 s^{-1} (Fig. S9), which is higher than that of SS-NFMO (1.16×10^{-9} cm^2 s^{-1}). This comparison indicates faster Na^+ diffusion in the CP-NFMO cathode than that in SS-NFMO. The cycling stability of the CP-NFMO-850 cathode was demonstrated up to 100 cycles at 1C (Fig. 4d). In contrast, the SS-NFMO cathode shows poor capacity after 100 cycles (Fig. S10). Moreover, it also exhibits a worse rate performance than the CF-NFMO cathode (Fig. S11). The post-cycling analysis was performed to characterize the crystal structures of both cathodes (CP-NFMO and SS-NFMO) after 100 charge/discharge cycles. The XRD results

(Fig. S12) reveal that a new diffraction peak at $2\theta = 18.02^{\circ}$ emerges for the SS-NFMO sample, which suggests a phase transition from P2 to a spinel phase upon repeated cycling. In contrast, the CP-NFMO cathode displays almost identical diffraction patterns to those of the pristine sample, indicating its structural stability during electrochemical cycling.

In summary, electrochemical and structural analyses confirm that the co-precipitation synthesis route yields superior $Na_{0.67}Fe_{0.5}Mn_{0.5}O_2$ cathodes compared to the solid-state synthesis method. Although both synthesis approaches generate a P2-type crystal structure, the CP-derived sample exhibits a finer particle size and homogeneous compositions as well as less Na loss after calcination, contributing to fast Na^+ diffusion. For the half cells, the co-precipitation-derived sample exhibits higher reversible capacity (135 mAh g^{-1} initial discharge capacity at 1C), slower capacity fading, supported by stable voltage profiles, reversible redox peaks and higher capacity retention. The post-cycling analysis reveals that the CP-NFMO sample exhibits higher structural stability upon repeated cycling. Overall, the co-precipitation approach enables better control over morphology and phase formation, resulting in improved Na^+ diffusion kinetics and superior electrochemical performance of sodium-ion batteries.

Conflicts of interest

There are no conflicts to declare.

Data availability

The data supporting this article have been included as part of the supplementary information (SI). Supplementary information: experimental section, SEM images, HRTEM images, TEM/STEM images, HAADF-STEM images, EDS spectra, dQ/dV curves, diffusion coefficients, and electrochemical cycling performance. See DOI: https://doi.org/10.1039/d6cc02378a.

Acknowledgements

This work was supported by the U.S. Department of Energy, Office of Science, Basic Energy Sciences under Award #DE-SC0024131.

References

1 Y. Zhang, G.-Q. Liu, Q. Sun, D. Qiao, J. Chen, L. Wen and M. Zhao, *J. Energy Storage*, 2024, **102**, 114279.
2 X. Liang, X. Song, H. H. Sun, H. Kim, M.-C. Kim and Y.-K. Sun, *Nat. Commun.*, 2025, **16**, 3505.
3 V. P. Mhaske, S. Jilkar and M. D. Yadav, *Energy Fuels*, 2023, **37**, 16221–16244.
4 B. Peng, Z. Zhou, J. Shi, X. Huang, Y. Li and L. Ma, *Adv. Funct. Mater.*, 2024, **34**, 2310925.
5 J. Liu, N. Zhang, H. Shi, Z. He, Z. Zhang, D. V. Anishchenko, E. V. Alekseeva, R. Li, P. Yang, O. V. Levin, D. Wang, H. Liu, S. Dou and B. Wang, *Chem. Eng. J.*, 2025, **521**, 167111.
6 C. Zhao, Q. Wang, Z. Yao, J. Wang, B. Sánchez-Lengeling, F. Ding, X. Qi, Y. Lu, X. Bai, B. Li, H. Li, A. Aspuru-Guzik, X. Huang, C. Delmas, M. Wagemaker, L. Chen and Y.-S. Hu, *Science*, 2020, **370**, 708–711.
7 S. Chu, S. Guo and H. Zhou, *Chem. Soc. Rev.*, 2021, **50**, 13189–13235.
8 T. Chen, B. Ouyang, X. Fan, W. Zhou, W. Liu and K. Liu, *Carbon Energy*, 2022, **4**, 170–199.
9 Q. Wang, S. Mariyappan, J. Vergnet, A. M. Abakumov, G. Rousse, F. Rabuel, M. Chakir and J.-M. Tarascon, *Adv. Energy Mater.*, 2019, **9**, 1901785.
10 G. Zhang, J. Li, Y. Fan, Y. Liu, P. Zhang, X. Shi, J. Ma, R. Zhang and Y. Huang, *Energy Storage Mater.*, 2022, **51**, 559–567.
11 R. Liu, W. Huang, J. Liu, Y. Li, J. Wang, Q. Liu, L. Ma, G. Kwon, S. N. Ehrlich, Y. Wu, T. Liu, K. Amine and H. Li, *Adv. Mater.*, 2024, **36**, 2401048.
12 W. Huang, T. Liu, L. Yu, J. Wang, T. Zhou, J. Liu, T. Li, R. Amine, X. Xiao, M. Ge, L. Ma, S. N. Ehrlich, M. V. Holt, J. Wen and K. Amine, *Science*, 2024, **384**, 912–919.
13 E. Boivin, R. A. House, J. J. Marie and P. G. Bruce, *Adv. Energy Mater.*, 2022, **12**, 2200702.
14 Y. Yang, Z. Wang, C. Du, B. Wang, X. Li, S. Wu, X. Li, X. Zhang, X. Wang, Y. Niu, F. Ding, X. Rong, Y. Lu, N. Zhang, J. Xu, R. Xiao, Q. Zhang, X. Wang, W. Yin, J. Zhao, L. Chen, J. Huang and Y.-S. Hu, *Science*, 2024, **385**, 744–752.
15 D. Wang, F. Zou, W. Lin, X. Zhang, X. Zhang, X. Qi, S. Xu, H. Mao, D. Xiao, S. Lu, B. Guo, Y. S. Hu and Y. Lyu, *Adv. Sci.*, 2025, DOI: 10.1002/advs.202501852.
16 Y. Niu, Z. Hu, B. Zhang, D. Xiao, H. Mao, L. Zhou, F. Ding, Y. Liu, Y. Yang, J. Xu, W. Yin, N. Zhang, Z. Li, X. Yu, H. Hu, Y. Lu, X. Rong, J. Li and Y. S. Hu, *Adv. Energy Mater.*, 2023, **13**, 2300746.
17 R. Qi, M. Chu, W. Zhao, Z. Chen, L. Liao, S. Zheng, X. Chen, L. Xie, T. Liu, Y. Ren, L. Jin, K. Amine, F. Pan and Y. Xiao, *Nano Energy*, 2021, **88**, 106206.
18 C. Hakim, N. Sabi and I. Saadoune, *J. Energy Chem.*, 2021, **61**, 47–60.
19 H. Xu, Q. Yan, W. Yao, C.-S. Lee and Y. Tang, *Small Struct.*, 2022, **3**, 2100217.
20 J. Lamb and A. Manthiram, *Chem. Mater.*, 2020, **32**, 8431–8441.
21 T. Deng, X. Fan, J. Chen, L. Chen, C. Luo, X. Zhou, J. Yang, S. Zheng and C. Wang, *Adv. Funct. Mater.*, 2018, **28**, 1800219.
22 A. T. Promi, J. Yao, D. Xia, C. Connor, A. U. Olayiwola, J. Bai, C. Sun, D. Nordlund, K. Zhao and F. Lin, *J. Mater. Chem. A*, 2025, **13**, 17063–17074.
23 L. Qian, R. Huang, H. Zhang, S. Yan and S. Luo, *ACS Appl. Energy Mater.*, 2024, **7**, 8136–8146.
24 V. K. Kumar, S. Ghosh, S. Biswas and S. K. Martha, *J. Electrochem. Soc.*, 2021, **168**, 030512.
25 N. Zhang, X. Fan, Y. Tong, M. Wang, H. Ding, J. Zhou, X. Li, D. Zhao and S. Li, *Ionics*, 2025, **31**, 1483–1497.
26 P.-F. Wang, Y. You, Y.-X. Yin and Y.-G. Guo, *Adv. Energy Mater.*, 2018, **8**, 1701912.
27 J. Jiao, E. Zhao, W. Yin, J. Che, Y. Cheng, Z. Xia, X. Xiao and X. Zhang, *Small*, 2024, **20**, 2308776.